Noise, transient dynamics, and the generation of realistic interspike interval variation in square-wave burster neurons

Bóris Marin[*]
Instituto de Física, Universidade de São Paulo, Brazil

Reynaldo Daniel Pinto[†]
Instituto de Física de São Carlos, Universidade de São Paulo, Brazil

Robert C. Elson[‡]
Institute for Nonlinear Science, University of California, San Diego, California 92093-0402, USA

Eduardo Colli[§]
Instituto de Matemática e Estatística, Universidade de São Paulo, Brazil

(Received 3 July 2014; published 20 October 2014)

First return maps of interspike intervals for biological neurons that generate repetitive bursts of impulses can display stereotyped structures (neuronal signatures). Such structures have been linked to the possibility of multicoding and multifunctionality in neural networks that produce and control rhythmical motor patterns. In some cases, isolating the neurons from their synaptic network reveals irregular, complex signatures that have been regarded as evidence of intrinsic, chaotic behavior. We show that incorporation of dynamical noise into minimal neuron models of square-wave bursting (either conductance-based or abstract) produces signatures akin to those observed in biological examples, without the need for fine tuning of parameters or *ad hoc* constructions for inducing chaotic activity. The form of the stochastic term is not strongly constrained and can approximate several possible sources of noise, e.g., random channel gating or synaptic bombardment. The cornerstone of this signature generation mechanism is the rich, transient, but deterministic dynamics inherent in the square-wave (saddle-node and homoclinic) mode of neuronal bursting. We show that noise causes the dynamics to populate a complex transient scaffolding or skeleton in state space, even for models that (without added noise) generate only periodic activity (whether in bursting or tonic spiking mode).

DOI: 10.1103/PhysRevE.90.042718 PACS number(s): 87.19.ll, 87.19.lc

I. INTRODUCTION

Working with bursting neurons from crustacean central pattern generators (CPGs), the authors of [1,2] made a striking observation: even though the interspike interval (ISI) sequences for different cell types were indistinguishable through histograms, plots of the $(n+1)$th ISI versus the nth ISI—or ISI *return maps*–were cell-type specific, even inside a fully connected and functional neural circuit. Further investigations demonstrated that ISI first return maps for biological neurons tend to reveal characteristic patterns of firing sequences for systems as diverse as crustacean stomatogastric (STG) neurons [1,2], mammalian retinal ganglion cells [3], and subthalamic neurons [4].

By construction, each burst containing M spikes contributes $M-2$ points to the ISI first return map. In the specific case of crustacean stomatogastric neurons, it turns out that such points tend to distribute over small specific regions of the ISI return plane, resulting in a specific arrangement of small clusters which are populated always in the same sequence, burst after burst. Such a specific geometrical arrangement of clusters was termed a *neuronal signature* in Refs. [1,2], since it allowed the identification of neuronal types in circuits presenting different bursting frequencies, duty cycles, and number of spikes per burst, even across biological species [5]. Moreover, this signature was shown to reflect circuit connectivity [1,2], information in synaptic input patterns [5], and the modulation of network operation [6]. In this paper, we present experimental ISI return maps containing such characteristic patterns and discuss geometrical mechanisms for their generation in conductance models.

In realistic electrophysiological neuronal models, several dynamical variables and parameters interact in nonlinear ways to produce complex activity patterns, such as quiescence, tonic spiking and bursting, which can even coexist for the same cell [7]. The spiking-bursting activity may be periodic or chaotic. A burst of spikes, taken as a whole, might function as a robust unit of neural information [8–11]. In contrast, the possibility of information coding *within* bursts has received little attention.

The information-processing properties of CPGs have been explored in model circuits inspired by the networks in the crustacean stomatogastric ganglion (STG) [12–14]. The authors proposed a CPG that generates a steady rhythm

[*]Present address: Department of Neuroscience, Physiology and Pharmacology, University College London, London, UK; bmarin@if.usp.br
[†]reynaldo@ifsc.usp.br
[‡]Present address: Department of Biology, Point Loma Nazarene University, San Diego, California 92106, USA; RobertElson@pointloma.edu
[§]colli@ime.usp.br

 ©2014 American Physical Society

of bursts but also responds to or recognizes the signatures produced by its individual neurons. Analysis in the STG has shown that there is a neuron-to-neuron flow of information within a bursting, rhythm-generating network [5].

The ISI return maps of many STG neurons change considerably when the cells are disconnected from their synaptic circuit. In these isolated neurons, the ISI sequences *within* each burst vary *between* bursts, this variation growing exponentially as bursts evolve and the spike train progresses [15]. This activity has been classified as chaotic bursting [16]. However, the neurophysiological mechanisms of this behavior have remained elusive. Detailed, conductance-based models generally produce regular activity when parameters are set to biologically plausible values [17]. Deterministic neuron models operating in chaotic regimes can generate irregular (nonperiodic, broad spectrum) time series, but their ISI return maps are highly structured, because chaotic trajectories are confined to particular regions of state space [18–21]. Moreover, the production of chaotic activity involves fine-tuning of model parameters in order to meet strict criteria, e.g., being close to spike-adding bifurcations [20].

In contrast, state-space trajectories generated by stochastic processes are not confined in this way, because noise is able to nudge a dynamical system to populate the transient scaffolding (skeleton) inherent in the dynamics. Accordingly, we here propose a mechanism to generate the ISI signature of irregularly bursting neurons based on the interplay of deterministic and stochastic dynamics. The noiseless system does not need to be tuned to a chaotic regime, nor is there a restrictive definition of the origin of the noise. We anticipate that this approach can be applied to other problems as well, such as burst alignment algorithms and noise-level estimation.

II. METHODS

A. Biological neurons: recordings and analysis

The stomatogastric nervous system was removed from spiny lobsters, *Panulirus interruptus*, and pinned out *in vitro* in standard *Panulirus* saline [15]. The STG, which contains the rhythm-generating pyloric circuit, remained connected to anterior ganglia whose descending modulatory influence sustain cellular bursting activity. The lateral pyloric (LP) or pyloric dilator (PD) neurons were disconnected from synaptic input from other pyloric circuit neurons by photoinactivating or deeply hyperpolarizing some presynaptic neurons and blocking inputs from others pharmacologically [22,23]. After synaptic isolation, neurons were impaled by two microelectrodes for independent current injection and membrane potential recording.

Experimental signature maps were obtained by using a double threshold technique to detect spike timing. A spike is detected when the membrane potential time series rises above a threshold value of -35 mV. To avoid spurious detections driven by experimental noise, new spike detection is allowed only after the membrane potential decreases and crosses a -38 mV reset threshold.

B. Neuron model

Our analysis made use of a tridimensional conductance-based neuronal model (1). This model has been introduced as a minimal model for square-wave bursting [24] and has been previously analyzed in Refs. [21,25]. It consists of a two-dimensional fast subsystem coupled to a one-dimensional slower one. The fast subsystem consists of a persistent sodium current with instantaneous activation I_{Nap}, and a potassium current I_{Kd}. The slow subsystem comprises the gating dynamic of an *M-type* potassium current I_{KM}. The biophysical parameters are listed in Table I.

TABLE I. Parameters for the currents in the deterministic simulations [Eq. (1)]. V_i are the ionic reversal potentials, $\bar{g}_i$ are maximum conductance densities, and τ_i are the timescales for each conductance. The steady-state activation functions are defined as $m_i^{\infty} = \{1 + \exp[(V_i^{1/2} - V)/k_i]\}^{-1}$, where V stands for the membrane potential. Other passive parameters are the membrane specific capacitance $C = 1\ \mu\mathrm{Fcm}^{-2}$ and a dc bias $I_{\mathrm{ext}} = 5\ \mu\mathrm{Acm}^{-2}$.

	Nap	Kd	KM	Leak
V_i (mV)	60	−90	−90	−80
$\bar{g}_i$ (mS cm^{-2})	20	9	5	8
$V_i^{1/2}$ (mV)	−19.9	−25	−21.2	
k_i (mV)	15	5	5	
τ_i (ms)		0.152	20	

$$
\begin{aligned}
C\dot{V} &= I_{\mathrm{ext}} - g_{\mathrm{leak}}(V - V_{\mathrm{leak}}) - \overbrace{\bar{g}_{\mathrm{Nap}} m_{\mathrm{Nap}}^{\infty}(V - V_{\mathrm{Nap}})}^{I_{\mathrm{Nap}}} \\
&\quad - \underbrace{\bar{g}_i m_i (V - V_{\mathrm{K}})}_{\mathrm{I}_i}, \qquad (1) \\
\dot{m}_i &= \frac{m_i^{\infty} - m_i}{\tau_i}, \quad i = [\mathrm{Kd,KM}].
\end{aligned}
$$

Bursting activity is generated via an hysteretic loop. It can be easily analyzed by considering the slow variable m_{KM} as a bifurcation parameter [24,26], which drives the fast subsystem cyclically from a branch of equilibria (henceforth denoted as $\mathcal{E}$) to a limit cycle manifold $\mathcal{L}$ (Fig. 1). When the trajectory (gray curve in Fig. 1) slides along the stable equilibrium part of $\mathcal{E}$ (solid segment of thin black line marked as $\mathcal{E}$), the full tridimensional system is in the hyperpolarized, interburst phase. Since the flux is evolving below the m_{KM} nullcline (long dashed red [gray] curve), it moves toward smaller m_{KM} values. The stable equilibrium eventually disappears in a saddle-node bifurcation (point labeled SN), so the trajectory moves towards the spiking manifold $\mathcal{L}$ (thick black "tube"). Crossing the m_{KM} nullcline leads the trajectories to move towards larger m_{KM} values. Spikes in the active phase of bursting correspond to full revolutions around $\mathcal{L}$. This manifold disappears in a saddle-homoclinic orbit bifurcation (point labeled S-H), when it collides with the middle (saddle) segment of $\mathcal{E}$.

Several conductance-based models can give rise to square-wave bursting, including those built to study systems as diverse as pancreatic β-cells [20,27], neurons in the pre-Bötzinger complex of the brain stem [28,29] or hippocampal CA1 pyramidal cells [30]. Our analysis can be applied to any of these or even other systems, provided that bursting involves a saddle middle branch in the equilibrium curve of the fast subsystem.

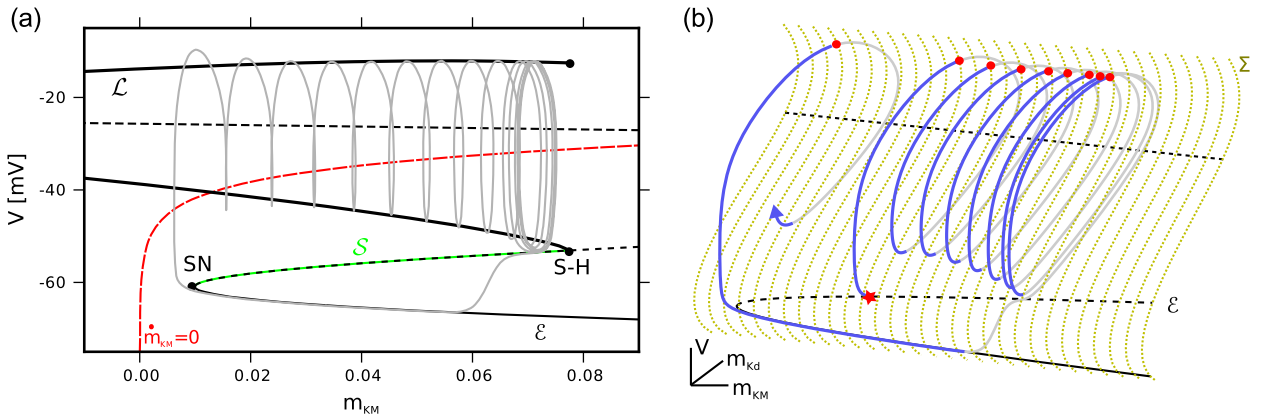

FIG. 1. (Color online) (a) Phase portrait for the noiseless neuronal model Eq. (1). A noiseless bursting trajectory is depicted in gray. The thin black curves correspond to the fast subsystem equilibrium branch $\mathcal{E}$, where solid (dashed) lines denote stable (unstable) states—saddles, in this case. The thick black "tube" depicts the envelope of the spiking manifold $\mathcal{L}$. The long dashed red (gray) curve is the $m_{\rm KM}$ nullcline: trajectories below (above) it move towards smaller (larger) $m_{\rm KM}$ values. Labelled points indicate bifurcations in the fast subsystem: SN: saddle-node and S-H: saddle-homoclinic orbit. The green (dashed black over light gray) curve defines the saddle middle branch $\mathcal{S}$, starting at the saddle node and ending at the homoclinic bifurcation. (b) Full-model trajectory (blue [dark gray] and light gray curves) emanating from initial condition (star) in the unstable manifold of a saddle in the saddle branch $\mathcal{S}$. The Poincaré surface of section Σ is depicted in dotted beige (gray). Filled circles represent Σ crossings, which are used in the reduced model analysis.

As additional examples of square-wave bursting neuron signatures, we have included those generated by the Hindmarsh–Rose three-dimensional model [31], with parameters as in Table II, and a model for neurons in the pre-Bötzinger complex (model and parameters described in Ref. [28], model 1). In both models, the chosen parameter set supported periodic bursting activity.

C. Stochastic dynamics

Stochastic ion channel gating has been suggested to be the major source of noise in isolated neurons [32]. Since our derivation of the generative model for ISI map signatures does not impose constraints nor require a particular noise mechanism, we chose to model stochastic gating using three different approaches [33]. For the Nap-Kd-KM model, we used a Langevin approximation to microscopic gating schemes derived in Ref. [34]. In this approximation, the subunit gating dynamics $\dot{m}_i$ are complemented with a state dependent (multiplicative) random forcing ξ, with zero mean and variance inversely proportional to the number of channels N in the membrane patch, according to Eq. (2):

$$\dot{m}_i = \frac{m_i^\infty - m_i}{\tau_i} + \xi_i, \quad \langle \xi_i \rangle = 0,$$
$$\langle \xi_i(t)\xi_i(t')\rangle = \frac{m_i^\infty(1-m_i^\infty)}{N_i\tau_i}\delta(t-t'). \tag{2}$$

For the Hindmarsh–Rose model, we opted for the current noise approach [33], adding a stochastic force directly to the membrane potential equation. Finally, for the pre-Bötzinger neuron model, we used conductance noise [33,34], where the stochastic terms are added to the conductance terms in the voltage dynamics: $I_i = \overline{g}_i(m_i + \xi_i)(V - V_i)$.

The resulting stochastic differential equations were integrated numerically by using the Euler–Maruyama scheme [35] with a fixed time step of 0.001 ms.

TABLE II. Parameter values for the Hindmarsh–Rose neuron model, periodic bursting mode.

a	b	c	d	s	x_1	r	I
1	2.7	1	5	4	−1.6	0.01	4

III. RESULTS

A. ISI maps of irregular bursting in biological neurons

The biological neurons, LP and PD, generated irregular spiking-bursting activity of the type shown by the excerpted time series in Fig. 4(c). Maps of the ISIs for spike trains within bursts are shown in the boxed areas of Fig. 2. The initial ISIs, from the start of bursts, are shown in Figs. 2(b) and 2(d). As the bursts evolve, the dispersion of corresponding sequential ISIs increases greatly. Bursts also vary in total number of spikes.

B. Unidimensional reductions of neuronal model

We now construct a hybrid (deterministic and stochastic) mechanism for generating ISI map signatures similar to those of biological neurons. It is convenient to start with unidimensional reductions of the model [Eq. (1)] to guide the intuition and then generalize to the full system. A number of different strategies for performing such reductions have been proposed [21,36,37], all of which could be equivalently employed. Our analysis relied on straightforward Poincaré mapping and fast-slow subsystem decomposition [26,36].

Since ISI signatures are defined in terms of subsequent maxima in membrane potential traces, the Poincaré surface of section Σ had to be constructed in a way that the time between crossings corresponded to intermaxima intervals for the variable V. Such a requirement was satisfied by adopting

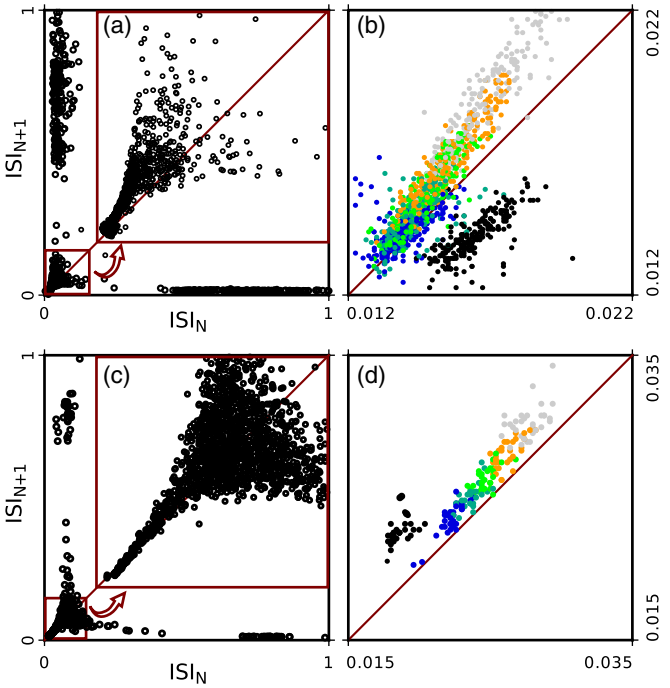

FIG. 2. (Color online) (a), (b) First return ISI maps for bursting activity of isolated LP and (c), (d) PD neurons from the STG of the lobster *Panulirus interruptus*. Colors (shades of gray) in panels (b) and (d) indicate successive ISI pairs at the start of bursts. ISIs have been normalized so that the maximum ISI is unity.

the surface defined by $\dot{V} = 0$ [see Fig. 1(b) for a schematic representation of Σ and a trajectory for the full model].

In the slow-fast decomposition, m_{KM} is treated as a control parameter for the fast subsystem. We built unidimensional maps characterizing the full dynamics by gridding the interval of m_{KM} values that supported limit cycles in the fast subsystem, and using intersections of Σ with these cycles as initial conditions for integrating the full system [Eq. (1)].

The discrete dynamics of m_{KM} in the intersection of the Poincaré surface of section Σ with the limit cycle manifold $\mathcal{L}$ is depicted in Fig. 3(a). The mapping $f_{1d}(m_{\mathrm{KM}})$ is the updated value of m_{KM} obtained by integrating the system along a cycle starting from the initial conditions described above, which provided us the (full model) time elapsed between each $\Sigma \cap \mathcal{L}$ crossing. Hence, we were able to couple an "observable" $\mathcal{T}\{m_{\mathrm{KM}}\}$ to the dynamics, giving rise to the map in Fig. 3(b). The ISI return map is then straightforwardly defined in terms of this observable, as the pairs $(\mathcal{T}\{m_{\mathrm{KM}}\}, \mathcal{T}\{f_{1d}(m_{\mathrm{KM}})\})$, displayed in Fig. 3(c).

C. Mechanism of noise-induced irregularity

The apparent discontinuity in the mapping f_{1d} is instrumental in understanding irregularities in the number of spikes and total burst duration. Notice that the dynamics is not chaotic: the strongly dissipative quasihorizontal segment ($m_{\mathrm{KM}} \approx 0.07$) reinjects all trajectories into neighboring points at the beginning of the spiking manifolds $\mathcal{L}$. Nevertheless it is possible—due to noise—that trajectories reach the almost vertical region of f_{1d}, being mapped leftward and climbing back up the spiking "ladder" (segment of f_{1d} with positive derivative). Thus, the large negative derivative in f_{1d} amplifies microscopic noise, leading to irregular ISI patterns and burst durations even when the noiseless system supports only periodic bursting.

Focusing back on the full model, it is possible to determine the origin of the abrupt, although continuous, change in f_{1d} after the fixed point m^*. There is an ensemble of states close to the end of the spiking manifold $\mathcal{L}$ that, when evolving towards hyperpolarization, follow the saddle branch of the equilibrium manifold $\mathcal{E}$—as depicted in Fig. 4(a)—and are eventually reinjected into the spiking manifold $\mathcal{L}$. In the membrane potential time series, such reinjections would be reflected as prolongation of bursts by addition of spikes or "burstlets": clusters of spikes appended to a bursting trajectory, after a hyperpolarization smaller than the typical interburst

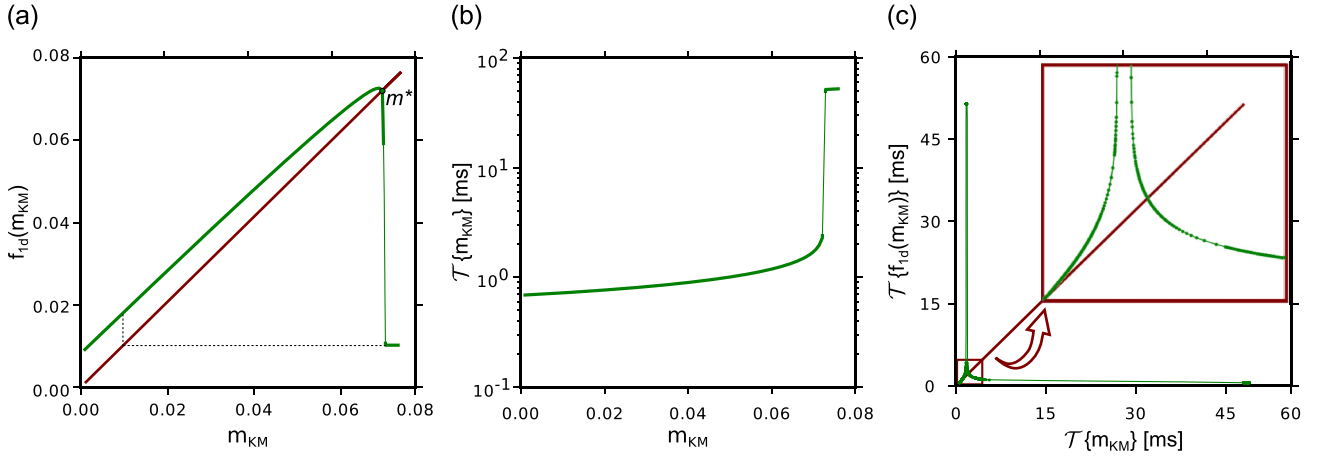

FIG. 3. (Color online) One-dimensional reduction of the dynamics. Panel (a) shows discrete dynamics $f_{1d}(m_{\mathrm{KM}})$ of the slow variable. The highly negative derivative section close to the fixed point m^* is of paramount importance in the suppression or addition of burstlets at the end of a burst, leading to complex ISI signatures. (b) The observable $\mathcal{T}\{m_{\mathrm{KM}}\}$ coupled to the dynamics in A, that encodes the (full model) time elapsed in a $f_{1d}(m_{\mathrm{KM}})$ mapping. (c) The ISI signature structure, defined in terms of the observable $\mathcal{T}\{.\}$. The thin lines connecting calculated points were added to guide the eye.

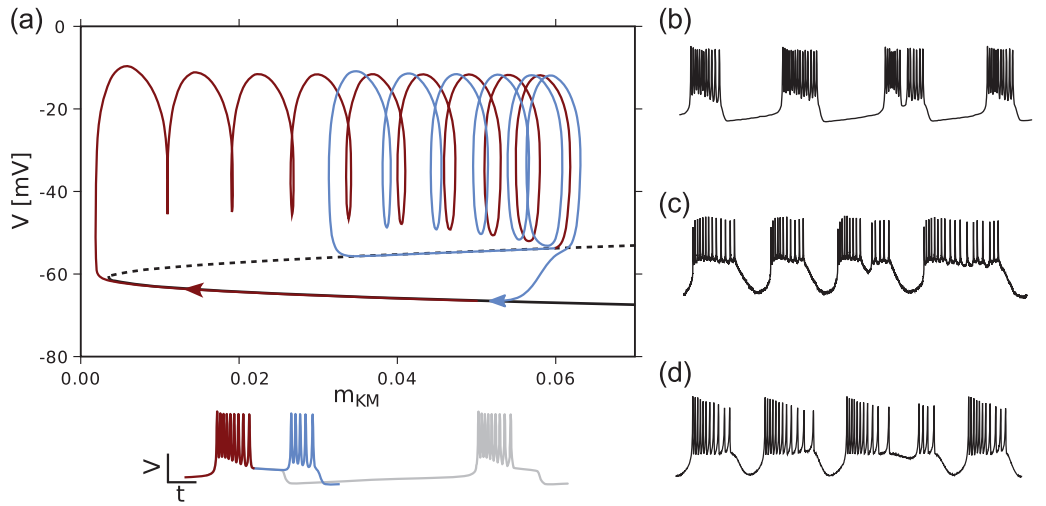

FIG. 4. (Color online) Burstlets associated with canard trajectories. (a) The red (dark gray) part of the trajectory indicates the bursting "main sequence," with the flux evolving through the spiking manifold $\mathcal{L}$. This particular trajectory does not fall directly to the stable part of the equilibria manifold (black curve) after $\mathcal{L}$ disappears in the homoclinic bifurcation. Instead, it glides along the unstable (saddle) branch of $\mathcal{E}$ (dashed black curve) for some time (blue [light gray] part of trajectory), until being reinjected into $\mathcal{L}$, thus generating a burstlet. The bottom traces represent the time course of the burstlet trajectory, superimposed with a regular (long trace in lighter gray) one. This trajectory was obtained by integrating the deterministic Nap-Kd-KM model for a parameter set close to a spike adding transition, so that a long "burstlet" could be easily obtained for the sake of illustration. (b)–(d) Burstlets in the stochastic Nap-Kd-KM model, a biological PD neuron and the stochastic Hindmarsh–Rose model, respectively.

hyperpolarization. Examples of such burstlets can be seen in Figs. 4(b)–4(d).

Trajectories that follow unstable structures such as the middle branch of $\mathcal{E}$ are called *canards* [38,39]. Note that these reinjections into $\mathcal{L}$ can take place at any m_{KM} value up to the vicinity of the saddle-node bifurcation, depending on how long the trajectory follows the saddle branch. It is precisely this set of transient canard orbits that gives rise to the "dynamical skeleton" of ISI signatures, the deterministic substrate that is populated when noise is added to the model. We will construct this "skeleton" in detail in the next section.

D. Skeleton of ISI signature map for full model

In order to unearth the skeleton, we first need to construct what we called a "flabellate structure" $\mathcal{W}$ in the Poincaré section Σ. We start by taking initial conditions over the unstable separatrices (approximated through the eigenvector corresponding to a positive eigenvalue) of points in the saddle middle branch $\mathcal{S}$. This branch is composed by saddle points in the fast subsystem equilibrium curve $\mathcal{E}$, between the fold (SN) and homoclinic (S-H) bifurcations, and is indicated in green (dashed black over light gray) in Fig. 1(a). One such initial condition is depicted as a star in Fig. 1(b), as well as the crossing it originates in Σ. The full system is then integrated until the first Σ crossing. Proceeding likewise for each one of the saddle points in $\mathcal{S}$, we obtain a set of intercepts $S \in \Sigma$, represented by the blue (dark gray, top) curve in Fig. 5. Let f be the discrete dynamics on Σ (the Poincaré map), i.e., the map which generates a sequence of Σ crossings according to the full model dynamics, analogously to f_{1d} for the reduced model. Each one of the points S in the blue (dark gray, top) curve is then iterated with f, producing a new set of Σ intercepts $f(S)$. This gives rise to the green (second from top to bottom) curve in Fig. 5. Accordingly, subsequent iterates $f^n(S)$ will generate the flabellated structure $\mathcal{W}$.

Notice that each one of the constituent branches of $\mathcal{W}$ (colored [shades of gray] curves in Fig. 5) starts with a black point, at its lowest m_{KM} value. Such points are the Σ

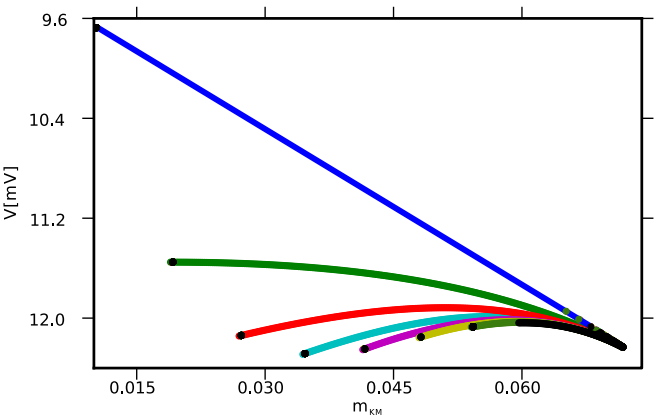

FIG. 5. (Color online) Projection into the $m_{\mathrm{KM}}V$ plane of the flabellate structure $\mathcal{W}$ generated inside the Poincaré section Σ. The blue (long dark gray, at the top) curve depicts Σ crossings for initial conditions close to the unstable manifolds of saddles in the $\mathcal{S}$ branch. The black circle at the end of the blue (dark gray, top) curve is visited every time a complete interburst hyperpolarization takes place, as happens to be the case for the nine-spike periodic orbit of the unperturbed model. The other colored (shades of gray, evolving counterclockwise from the long dark gray curve at the top) curves are $m_{\mathrm{KM}}V$ projections of the iterates of states in the blue (dark gray, top) curve under the Poincaré map associated with section Σ. Their (left, black) endpoints are the iterates of the left endpoint of the blue (dark gray, top) curve.

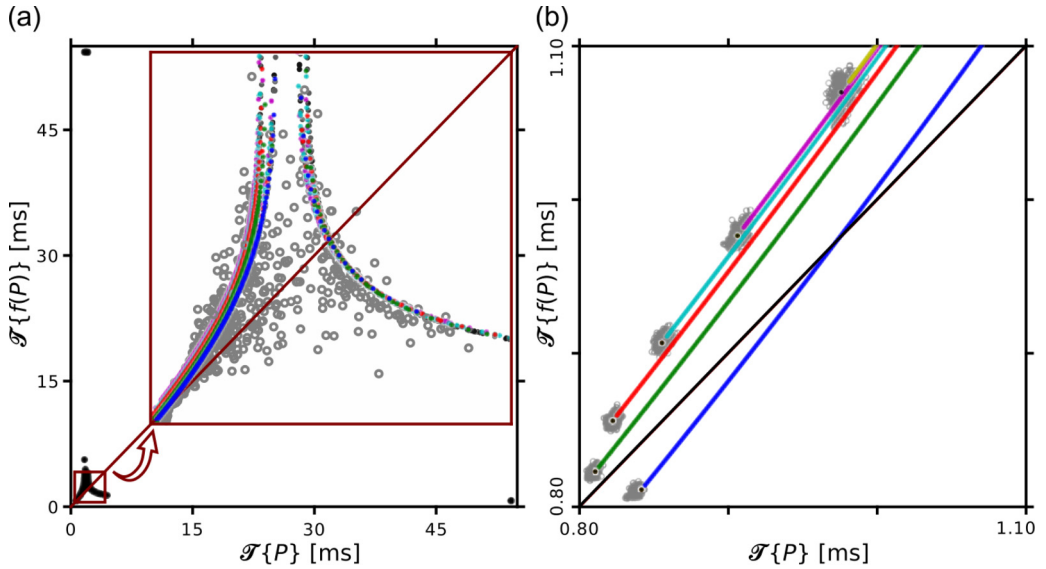

FIG. 6. (Color online) (a), (b) Signature skeleton (colored [shades of gray] filled circles): $(\mathscr{T}\{P\}, \mathscr{T}\{f(P)\})$ pairs for points P in the flabellate structure $\mathcal{W}$ of Fig. 5. The generated "infrastructure" is only accessible by the system through the addition of noise, given the strongly attractive character of the periodic bursting orbit. The unfilled gray circles correspond to a signature generated by simulating the stochastic model. Panel (b) depicts the cluster generation mechanism for the first ISIs in a burst, along the deterministic scaffolding (colored [shades of gray] curves emerging from clusters centered at the periodic orbit for the noiseless case).

intersections of the periodic orbit for the unperturbed system. The flabbelate form $\mathcal{W}$ reveals a dynamically rich, transient infrastructure that can be visited when the system is perturbed by noise, but lies "hidden" in the noiseless case.

Now let $\mathscr{T}$ be the function with domain in Σ and assuming values in the positive real numbers, which gives the time needed for a point in Σ to return to it under the full dynamics. This is the natural extension, in the full model, of the return time $\mathcal{T}$ used in the unidimensional reduction. The level curves of $\mathscr{T}$ will be called *isochrons*.

If P_n is the nth intersection of the trajectory with Σ [examples depicted in Fig. 1(b)], then $f(P_n)$ is the next intersection, $\mathscr{T}\{P_n\}$ will be the interspike duration (nth ISI), and $\mathscr{T}\{P_{n+1}\}$ will be the next interspike duration [$(n+1)$th ISI]. This establishes a relation between Σ and an ISI return diagram, by the map $P \mapsto (\mathscr{T}\{P\}, \mathscr{T}\{f(P)\})$, or the *ISI return map transformation*.

When noise is taken into account, the otherwise periodic orbit is perturbed and there is an increased probability of trajectories being reinjected into the spiking manifold $\mathcal{L}$ via the burstlet mechanism, i.e., transient orbits through unstable manifolds of saddles in the middle branch $\mathcal{S}$. This way, the blue (dark gray, top) curve in Fig. 5 will be populated, and subsequently the flabellate structure $\mathcal{W}$. Then the regions of the ISI diagram most likely to be visited are in the image of $\mathcal{W}$ under the ISI return map defined above, i.e., $(\mathscr{T}\{\mathcal{W}\}, \mathscr{T}\{f(\mathcal{W})\})$. This construction is termed the *signature skeleton* and is depicted in Fig. 6.

In the noiseless case, due to the attracting periodic orbit, the signature structure [defined as all the $(\mathscr{T}\{P\}, \mathscr{T}\{f(P)\})$ pairs for points P in the periodic orbit] will correspond only to the images of the endpoints of $\mathcal{W}$ (black circles, Fig. 5, corresponding to solid colored [shades of gray] points in Fig. 6). When noise is taken into account, stereotypical clusters akin to the ones observed in experimental signatures arise along the deterministic infrastructure [Fig. 6(b)]. Notice that, for the initial spikes in every new burst, the sequence of population of each cluster is likely to be the same, according to the order of each "bone" [colored (shades of gray) lines in Fig. 6(b)] in the skeleton.

Fig. 7 represents the dynamics in Σ projected onto the $m_{\mathrm{KM}}V$ plane, with the addition of first return isochrons. An isochron is a subset of Σ with constant return time. In Fig. 7, a color (shade of gray) was assigned to each isochron. The origin of the hook-shaped structure ("kink") for the smallest ISI in the experimental signatures [Figs. 2(b) and 2(d) black-blue-green (black-increasingly lighter shades of gray) sequence] is elucidated by noticing that noise tends to spread crossings across isochrons. This way, two ISI in different positions along the burst are similar, leading to vertically stacked clusters in the $(\mathscr{T}\{P\}, \mathscr{T}\{f(P)\})$ (signature) map.

E. Simulation of ISI map signatures

The integration of the full (noisy) model [Eqs. (1) and (2)], in addition to a simple threshold (-30 mV) spike detection, leads to the ISI signature map in Fig. 8. This map qualitatively reproduces the structure of the ISI signature of biological neurons (Fig. 2), including fine details such as the kink in the low-ISI main sequence, as well as the variability in both number of spikes and interburst intervals (reflected in the diffusiveness at the end of the main sequence and the extent of the isolated high-ISI arms). All of these features can be traced back to an underlying deterministic scaffolding, so that the role of noise is to induce transient dynamics exposing this infrastructure. Note also that the qualitative resemblance between model and biological ISI maps was obtained without special tuning of model parameters. Similar structures were

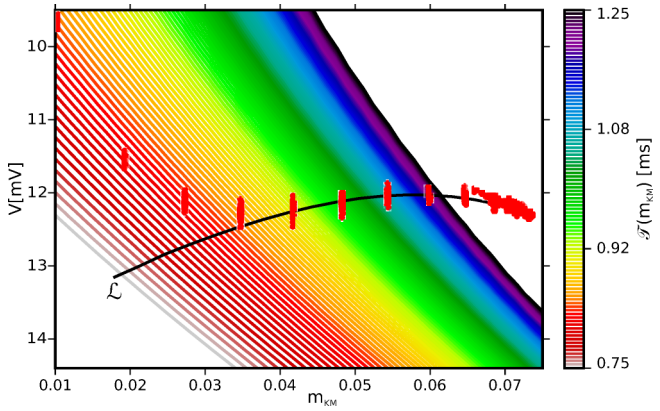

FIG. 7. (Color online) Isochrons of return time to Σ. Long times (blank areas) have been discarded to increase readability. The black curve is the intersection of the surface of section Σ with the fast subsystem limit cycle manifold $\mathcal{L}$, corresponding to intraburst spiking. Red (clustered dark gray) circles correspond to Σ crossings of an integrated trajectory of the full noisy model [Eqs. (1) and (2)]. Noise tends to spread the crossing points across isochrons, so that spikes of different positions in a burst give rise to similar ISIs—generating "kinks" in the signature. Grayscale: starting from the 0.75 ms isochron on the bottom left, return times grow monotonically following isochrons from left to right towards the rightmost isochron (black, 1.25 ms return time).

also obtained by adding noise to either pre-Bötzinger or Hindmarsh–Rose model neurons (Fig. 9), suggesting that similar mechanisms may be at work in these cases also.

IV. DISCUSSION

The presented mechanism accounts for the generation of irregular bursting traces with complex signatures, in terms of a low-dimensional conductance-based model and a macroscopic approximation of stochastic gating noise. Noise plays a crucial role in the mechanism: although the deterministic scaffolding of the model (its skeleton) can support complex behavior, this dynamical richness is usually suppressed by the dissipative character of the periodic bursting or tonic spiking orbits. Noise, however, unveils the transient dynamics, giving flesh

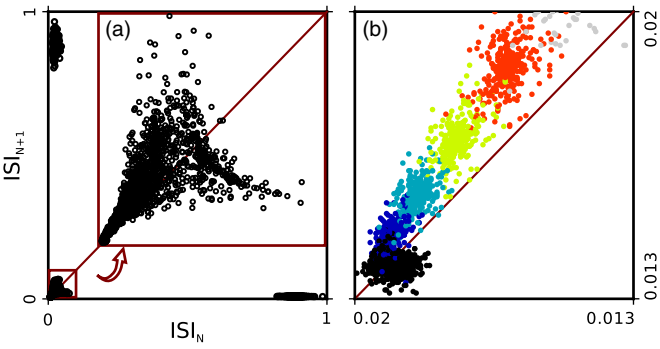

FIG. 8. (Color online) ISI signature generated by the model of a square-wave burster neuron with channel noise [Eqs. (1) and (2)]. Scaling of plots and point colors as in Fig. 2.

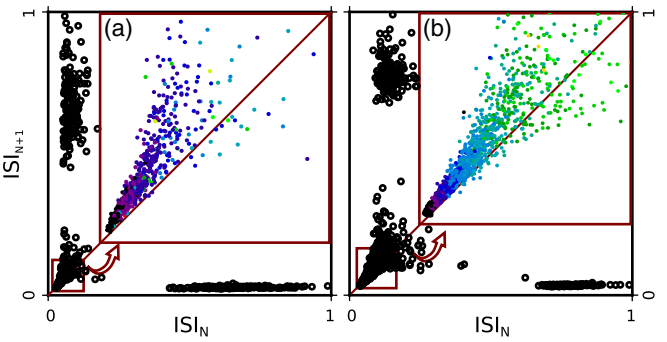

FIG. 9. (Color online) (a) Signature generated by the pre-Bötzinger neuron model with conductance noise. (b) Signature generated by the Hindmarsh–Rose neuron model with current noise. Conventions are as in Figs. 2 and 8.

to the skeleton and generating the ISI signature patterns characteristic of biological neurons.

Let Σ be the hypersurface defined by $\dot{V} = 0$. Let $\mathcal{S}$ be the set of saddle points between the saddle-node and homoclinic bifurcations in the equilibrium branch $\mathcal{E}$. The set of intersections of Σ with the unstable manifolds of the saddles in $\mathcal{S}$ and further iterates of these intersections under the Poincaré mapping $f : \Sigma \to \Sigma$ define the flabellate structure $\mathcal{W}$. Now consider the observable $\mathcal{T} : \Sigma \to \mathbb{R}^+$, which gives the return time to Σ. Skeletons are the image of the ISI return map transformation when applied to $\mathcal{W}$, i.e., the pairs $(\mathcal{T}\{\mathcal{W}\}, \mathcal{T}\{f(\mathcal{W})\})$.

We emphasize the robustness of the skeleton to parameter fluctuations: since it is inherently tied to the bifurcation structure of the model, its general features persist even through bursting-tonic transitions (associated with the gain of stability of the fixed point in the unidimensional map f_{1d}). Signatures essentially will remain the same for scenarios in which bursting is induced by noise (the noiseless system otherwise spiking tonically) [25]. That seems indeed to be the case for the PD neuron [Fig. 2(b)], given the presence of very long (more than 100 spikes) bursts and comparatively shorter hyperpolarization periods.

Irregular activity in neuronal models has been associated with the presence of deterministic chaos [40–42]. Nevertheless, the main cause of irregularities in our model is the amplification of stochastic phenomena by the transient dynamics. Structures defined by such dynamics persist even for parameter regimes that do not support chaotic attractors. Noise-induced chaos [43]—where the neighborhood of nonattracting hyperbolic sets is visited due to perturbations—could be present, because chaotic saddles can arise in spike-adding transitions as shown in Ref. [20]. This would, however, involve fine tuning of parameters and might prove too delicate to detect [44] with large noise intensities such as those needed, seemingly, to simulate biological results. Similar considerations may apply also to "stochastic chaos" associated with D-type stochastic bifurcations [45].

Bursting activity can be generated through several distinct geometric mechanisms [24] in addition to the saddle-node and homoclinic behavior studied here. By using the proposed geometrical framework, general features of the dispersion of ISI pairs in neuronal signature maps can be predicted. In

particular, the burstlet generation mechanism via transient canard trajectories will require bursting scenarios involving a saddle middle branch.

As different levels of noise are added to the model, there is a scaling of ISI cluster dispersion (data not shown). This provides a possible method of estimating the dynamical noise level in time series analysis of real neurons. We also point out that the burstlet definition and description can be used to improve burst alignment algorithms [46], by separating bursts into a "main sequence" followed by irregular burstlets.

ACKNOWLEDGMENTS

Financial support from the Brazilian agencies Fundação de Amparo à Pesquisa do Estado de São Paulo (FAPESP), Coordenação de Aperfeiçoamento de Pessoal de Nível Superior (CAPES), and the Conselho Nacional de Desenvolvimento Científico e Tecnológico (CNPq) is gratefully acknowledged. R.C.E. was supported by a grant from the National Science Foundation. We thank Geoffrey Evans for useful feedback on the manuscript.

[1] A. Szücs, R. D. Pinto, M. I. Rabinovich, H. D. I. Abarbanel, and A. I. Selverston, J. Neurophysiol. **89**, 1363 (2003).
[2] A. Szücs, H. D. I. Abarbanel, M. I. Rabinovich, and A. I. Selverston, Euro. J. Neurosci. **21**, 763 (2005).
[3] G. M. Zeck and R. H. Masland, Euro. J. Neurosci. **26**, 367 (2007).
[4] L. Garcia, G. D'Alessandro, P.-O. Fernagut, B. Bioulac, and C. Hammond, J. Neurophysiol. **94**, 3662 (2005).
[5] L. Brochini, P. V. Carelli, and R. D. Pinto, J. Neurosci. **31**, 12297 (2011).
[6] Y. Zhurov and V. Brezina, J. Neurosci. **26**, 7056 (2006).
[7] B. Marin, W. H. Barnett, A. Doloc-Mihu, R. L. Calabrese, and G. S. Cymbalyuk, PLoS Comput. Biol. **9**, e1002930 (2013).
[8] J. Lisman, Trends Neurosci. **20**, 38 (1997).
[9] B. Doiron, M. J. Chacron, L. Maler, A. Longtin, and J. Bastian, Nature (London) **421**, 539 (2003).
[10] E. M. Izhikevich, N. S. Desai, E. C. Walcott, and F. C. Hoppensteadt, Trends Neurosci. **26**, 161 (2003).
[11] A.-M. M. Oswald, M. J. Chacron, B. Doiron, J. Bastian, and L. Maler, J. Neurosci. **24**, 4351 (2004).
[12] F. de Borja Rodríguez, R. Latorre, and P. Varona, *Artificial Neural Networks–ICANN 2002*, edited by J. R. Dorronsoro, Lecture Notes in Computer Science Vol. 2415 (Springer, Berlin, Heidelberg, 2002), pp. 167–173.
[13] R. Latorre, F. de Borja Rodríguez, and P. Varona, Biol. Cybern. **95**, 169 (2006).
[14] A. Tristan, F. De Borja Rodriguez, E. Serrano, and P. Varona, Neurocomputing **58–60**, 41 (2004).
[15] R. C. Elson, R. Huerta, H. D. I. Abarbanel, M. I. Rabinovich, and A. I. Selverston, J. Neurophysiol. **82**, 115 (1999).
[16] A. I. Selverston, M. I. Rabinovich, H. D. I. Abarbanel, R. Elson, A. Szücs, R. D. Pinto, R. Huerta, and P. Varona, J. Physiol. (Paris) **94**, 357 (2000).
[17] A. A. Prinz, C. P. Billimoria, and E. Marder, J. Neurophysiol. **90**, 3998 (2003).
[18] J. Guckenheimer and R. A. Oliva, J. Appl. Dyn. Syst. **1**, 105 (2002).
[19] A. L. Shilnikov, R. L. Calabrese, and G. Cymbalyuk, Phys. Rev. E **71**, 056214 (2005).
[20] D. Terman, SIAM J. Appl. Math. **51**, 1418 (1991).
[21] G. S. Medvedev, Phys. Rev. Lett. **97**, 048102 (2006).
[22] J. P. Miller and A. I. Selverston, J. Neurophysiol. **48**, 1416 (1982).
[23] T. Bal, F. Nagy, and M. Moulins, J. Comp. Physiol., A **163**, 715 (1988).
[24] E. M. Izhikevich, Int. J. Bifurcation Chaos Appl. Sci. Eng. **10**, 1171 (2000).
[25] P. Hitczenko and G. Medvedev, SIAM J. Appl. Math. **69**, 1359 (2009).
[26] N. Fenichel, J. Differ. Equations **31**, 53 (1979).
[27] T. R. Chay and J. Keizer, Biophys. J. **42**, 181 (1983).
[28] R. J. Butera, J. Rinzel, and J. C. Smith, J. Neurophysiol. **82**, 382 (1999).
[29] J. Best, A. Borisyuk, J. Rubin, D. Terman, and M. Wechselberger, J. Appl. Dyn. Syst. **4**, 1107 (2005).
[30] D. Golomb, C. Yue, and Y. Yaari, J. Neurophysiol. **96**, 1912 (2006).
[31] J. L. Hindmarsh and R. M. Rose, Proc. R. Soc. London, Ser. B **221**, 87 (1984).
[32] P. F. Rowat and R. C. Elson, J. Comput. Neurosci. **16**, 87 (2004).
[33] J. H. Goldwyn and E. Shea-Brown, PLoS Comput. Biol. **7**, e1002247 (2011).
[34] R. F. Fox, Biophys. J. **72**, 2068 (1997).
[35] P. Kloeden and E. Platen, *Numerical Solution of Stochastic Differential Equations* (Springer-Verlag, Berlin, 1992).
[36] G. Medvedev, Physica D **202**, 37 (2005).
[37] P. Channell Jr., G. S. Cymbalyuk, and A. L. Shilnikov, Neurocomputing **70**, 2107 (2007).
[38] H. G. Rotstein, S. Coombes, and A. M. Gheorghe, J. Appl. Dyn. Syst. **11**, 135 (2012).
[39] J. Burke, M. Desroches, A. M. Barry, T. J. Kaper, and M. A. Kramer, J. Math. Neurosci. **2**, 3 (2012).
[40] M. Falcke, R. Huerta, M. I. Rabinovich, H. D. Abarbanel, R. C. Elson, and A. I. Selverston, Biol. Cybern. **82**, 517 (2000).
[41] P. V. Carelli, M. B. Reyes, J. C. Sartorelli, and R. D. Pinto, J. Neurophysiol. **94**, 1169 (2005).
[42] P. Channell Jr., I. Fuwape, A. B. Neiman, and A. L. Shilnikov, J. Comput. Neurosci. **27**, 527 (2009).
[43] Z. Liu, Y.-C. Lai, L. Billings, and I. B. Schwartz, Phys. Rev. Lett. **88**, 124101 (2002).
[44] J. B. Gao, C. C. Chen, S. K. Hwang, and J. M. Liu, Int. J. Mod. Phys. B **13**, 3283 (1999).
[45] E. K. Kosmidis and K. Pakdaman, Int. J. Bifurcation Chaos Appl. Sci. Eng. **16**, 395 (2006).
[46] L. F. Lago-Fernández, A. Szücs, and P. Varona, Neural Comput. **21**, 973 (2009).